Research Article Vol. 16, No. 4 / 1 Apr 2026 / Optical Materials Express 765
Optical Materials EXPRESS

Characterization of optothermal transition dynamics in $Ge_2Sb_2Te_5$ and Sb_2Te_3 via spatial light modulation microscopy

Robert E. Coleman Jr.,[1] Malcolm Bogroff,[1] Seppe Van Dyck,[2] Christophe Detavernier,[2] Sami Znati,[3] Parsian K. Mohseni,[3] and Eric Seabron[1,*]

[1]Department of Electrical and Computer Engineering, Howard University, Washington, D.C. 20059, USA
[2]Department of Solid State Sciences, Ghent University, Ghent, Belgium
[3]Microsystems Engineering, Rochester Institute of Technology, Rochester, NY 14623, USA
[*]eric.seabron@howard.edu

Abstract: We present a confocal microscopy-based method for constructing power-dependent optothermal transition (OTT) diagrams of phase-change chalcogenide (PCC) thin films via spatial light modulation, without diffraction-limited optics, pulse shaping, or temporal modulation. Optical dosage is engineered through controlled scanning dynamics to systematically map amorphous, crystalline, semi-crystalline, and failure regimes in $Ge_2Sb_2Te_5$ and Sb_2Te_3 on silicon and silicon-on-insulator substrates. Substrate-dependent transition setpoints and cycling behavior are identified and supported by optothermal simulations, while failure mechanisms, including delamination and dewetting, are experimentally resolved through spatially mapped optical measurements. Reproducible intermediate optical states are achieved through controlled variations in incident power and exposure count. Integration of two-photon excitation fluorescence and second-harmonic generation probes enable single-step discrimination between phase transitions and degradation, while revealing dynamic nonlinear behavior within the crystalline phase. This scalable optical platform advances PCC materials characterization and programming for photonic memory and reconfigurable integrated photonics.

1. Introduction

Phase-Change Chalcogenide (PCC) materials have garnered significant interest for photonic memory [1–7], neuromorphic computing [1,8], and optical reconfigurability [2,3,5,8–17] due to their non-volatile structural transitions. Optothermal programming of PCC devices using free space optics eliminates the electronic layer allowing for faster photonic READ/WRITE operations [1,2,18] and direct probing of intrinsic behavior [19–21]. Utilizing a free space laser beam to map the complex, multidimensional crystalline transition space offers a versatile approach for rapid calibration, tuning, and prototyping of PCC integrated devices. Conventional methods such as Time–Temperature–Transformation diagrams have been used to study crystallization dynamics in PCCs, enabling PCC phase switching [22–26]. In addition, methods for thermal engineering of samples in conjunction with laser pulse shaping have demonstrated robust cyclability in Sb_2Se_3 thin films with improved endurance [27]. Recent demonstrations leverage temporally modulated single pulse excitation, which employ complex optics such as pulse pickers, to enable reversible switching in PCCs [28–33].

In this work, we present a technique for extracting power dependent Optothermal Transition (OTT) diagrams of arbitrary PCCs thin films without the need for diffraction limited optics, complex pulse shaping, temporal modulation, or thermal engineering of the thin film stack. Our experimental framework leverages the mechanics of a confocal microscope to engineer optical dosage (number of pulses per unit area), enabling robust and reversible phase transitions in PCCs.

#589728 https://doi.org/10.1364/OME.589728
Journal © 2026 Received 8 Jan 2026; revised 18 Feb 2026; accepted 21 Feb 2026; published 2 Mar 2026

Optical Materials EXPRESS

Spatially resolved images of PCC thin films using both reflectance and non-linear emission probes are acquired simultaneously to gain insight into thin film failure mechanisms and non-trivial crystalline phase dynamics. Our analysis of experimental results is used to extract OTT diagrams, which reveal empirical trends in the intrinsic behavior of PCCs. We demonstrate OTT diagrams in the Near-Infrared for conventionally used $Ge_2Sb_2Te_5$ and underexplored Sb_2Te_3 [15,16] on both Silicon and Silicon-on-Insulator (SOI) substrates, showcasing unique cycling behavior, failure mechanisms, intermediate (analog-like) transitions, and non-linearity via Two-Photon Excitation Fluorescence (TPEF) and Second Harmonic Generation (SHG) microscopy.

2. Optothermal spatial light modulation

This technique enables the systematic exploration of all degrees of freedom associated with driving optothermal phase transitions using a free space laser, including dosage (number of pulses per unit area), average power density (mW/μm^2), and wavelength (λ). The pulse train is engineered and functionalized using spatial light modulation derived from mechanisms commonly found in confocal microscopy setups, depicted in Fig. 1(a). The spatial light modulation is driven by the confocal microscope's galvomirrors which scan the laser over a virtual "pixel grid." When considering a laser beam diameter larger than the thermal diffusion length scale (>1um), the optical dosage can be determined directly from the convolution of the beam's spatial profile (diameter and shape), centerline velocity (mm/sec), and laser pulse train (Hz). The average power density can be controlled independent of the spatial light modulation, only limited by the laser's peak power (mW) and resolution of the microscope objective. Our experimental setup for spatial light modulation utilizes a Ti:Sa Laser with a 140fs pulse width at 80 MHz and an ~6.5 um gaussian beam. The "High Pulse (HP)" configuration drives amorphous-to-crystalline transitions using ~222 pulses per exposure with a 7.7 mm/s beam velocity for a prolonged pixel dwell time. The "Low Pulse (LP)" configuration drives crystalline-to-amorphous transitions using ~12 pulses per exposure with a 656.1 mm/s beam velocity for a comparatively shorter pixel dwell time.

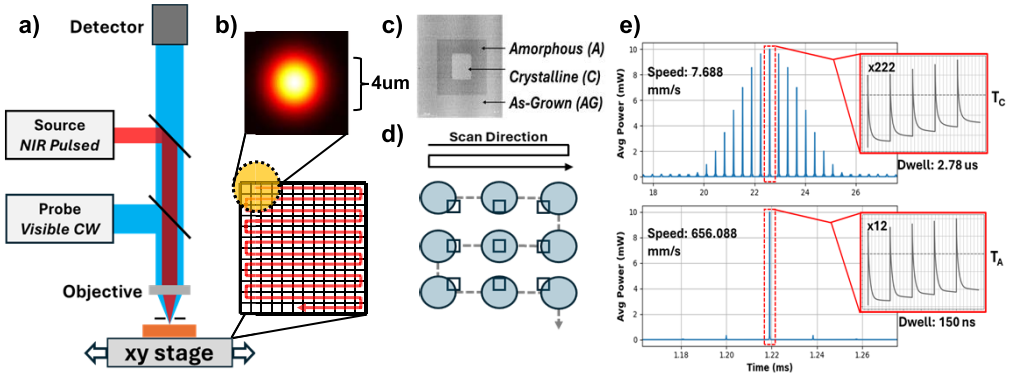

Fig. 1. Confocal Spatial-Temporal Modulation. **a)** Experimental Setup consists of a commercially available confocal microscope (Leica TCS SP8 MP) with an 80 MHz pulsed probe laser source (Leica WLL Laser) emitting in the visible range (470–670 nm) and a 140-femtosecond pulsed Ti:Sa laser source (Chameleon Vision MP II) emitting in the near IR (680-1080 nm). The Leica TCS SP8 MP has both photomultiplier and hybrid detectors, detecting in the range of 380-800 nm with a minimum bandwidth of 5 nm. **b)** Heatmap showing the Power Density of an 800 nm Airy Disk, **c)** Reflectance Image of $Ge_2Sb_2Te_5$, **d)** Serpentine Scanning Pattern, **e)** Pulse Train seen by a single pixel at the center of the scanning grid for High Pulse (above) and Low Pulse (below) configurations.

The spectral image information is collected concurrently while the pump laser drives the optothermal phase transitions, where pixel intensity corresponds to the number of photons

Optical Materials EXPRESS

reflected from the pump source itself, reflectance by colinear probe source, or spectra from non-linear emission, for each pixel in the "pixel grid". This data forms a spatially resolved probe image of the thin film, allowing visualization of PCC phase and failure mechanisms. Noise introduced by laser fluctuations and sample inhomogeneity is significantly suppressed by extracting the difference between the target and adjacent as-grown (AG) regions obtained simultaneously in the image data, as illustrated in Fig. S2. When image data is partitioned into these regions, we take the average of the number of reflected photons from every pixel in that defined region. This method has an advantage over commonly used single spot measurements because it isolates the change in reflectivity attributed to the phase change layer and reduces sensitivity to sample variation, probe laser jitter, and thermal gradient effects. Differential Reflectance (ΔR) is obtained by dividing the difference in the number of photons between the measured target area and the AG region by the number of photons reflected by a mirror standard (99.8% at 480 nm); $\Delta R = \frac{measured\ \#\ of\ photons - AG\ region\ \#\ of\ photons}{total\ \#\ of\ photons}$. We do not assume that the laser exposure is such that the optical properties and thickness of other sample layers are unchanged as this assumption is not necessary. Our normalization method for differential reflectance is not sensitive to this, as it removes the effects of these types of variations. Differential reflectance data can be combined and plotted as a function of incident average power density to quantify the PCC's dynamic optical behavior. Optothermal Transition (OTT) diagrams map changes in a material's reflectance with incident optical power density. They enable identification of incident power setpoints and conditions for phase transitions, supporting precise tuning of reconfigurable metasurfaces [1,7,10,34,35], optical switches [1,12,18], spatial light modulators [1,9,34], and tunable filters [36].

Using COMSOL Multiphysics, we created models that simulate the optothermal heating of $Ge_2Sb_2Te_5$ and Sb_2Te_3 on Silicon and Silicon-on-Insulator Substrates (See Supplement Section, Fig. S3). According to literature, we expect the threshold temperatures for $Ge_2Sb_2Te_5$ to be 150 C° for crystalline transition [37,38] and 600 C° for amorphous transition [39–41]; and for Sb_2Te_3 to be 227 C° for crystalline transition [42] and 620 C° for amorphous transition [43–45]. In our model, we map the time dependent temperature profile based on single pulse excitation, with incident power density comparable to those found in experimental results; the peak temperature and power densities are summarized in Table 1. For all models, we observe that for both transitions, the sample rapidly cools to near room temperature after each pulse, resembling the "Melt-Quench" temperature profile needed to reach amorphous transition temperatures for a short time-period without recrystallizing the sample. From our simulation results (Table 1, Fig. S3) we expect our technique can be used to reach adequate temperatures needed to induce phase transitions in $Ge_2Sb_2Te_5$ and Sb_2Te_3.

Table 1. Optothermal simulation results for single pulse heat generation

		Amorphous to Crystalline		Crystalline to Amorphous	
PCC	Substrate	Power Density ($mW/\mu m^2$)	Peak Temperature	Power Density ($mW/\mu m^2$)	Peak Temperature
$Ge_2Sb_2Te_5$	Silicon	0.279	511 C°	1.197	1453 C°
$Ge_2Sb_2Te_5$	SOI	0.074	310 C°	0.246	702 C°
Sb_2Te_3	Silicon	0.365	371 C°	1.337	2370 C°
Sb_2Te_3	SOI	0.289	142 C°	1.034	872 C°

3. Results: optothermal transition (OTT) diagrams

We outline a step-by-step method to identify the optimal parameters for crystalline and amorphous transitions in PCC thin films using our spatial light modulation technique. First, we select our

Optical Materials EXPRESS

probe wavelength to be 480 nm, guided by ellipsometry (Fig. S4), simulation (Figs. S5, S6, and S7), and analytical reflection modelling (Fig. S8) of our PCC stacks. In these simulations and models, we assume constant layer thickness and optical properties to isolate the specific reflection effects of the phase transition. Optical reflection simulations vary real and imaginary refractive indices independently, as well as SiO_2 cladding thickness with fixed refractive indices corresponding to crystalline and amorphous phases. Analytical reflection modelling predicts optical contrast between amorphous and crystalline phases of 2.77% for $Ge_2Sb_2Te_5$ on Silicon, 4.19% for $Ge_2Sb_2Te_5$ on SOI, 1.06% for Sb_2Te_3 on Silicon, and 2.75% for Sb_2Te_3 on SOI. Next, we identified the optimal pump wavelength for our PCCs using the HP configuration at four laser lines (680 nm, 800 nm, 920 nm, and 1060 nm) spanning the tunable near-infrared source. After each exposure (full scan of the pixel grid), a probe image was acquired, and the resulting differential reflectance data are shown in Fig. S9 These sweeps were conducted with the PCC in its as-grown state. Increases in differential reflectance indicate higher refractive index and crystalline transition, while decreases at elevated power correspond to failure; minimal increases imply weak absorption. This procedure was repeated for $Ge_2Sb_2Te_5$ and Sb_2Te_3 on silicon using the same probe wavelengths. We found that a pump wavelength of 800 nm was best for $Ge_2Sb_2Te_5$ samples and 920 nm was best for Sb_2Te_3 samples. A detailed description of the OTT diagrams is discussed in the Supplement Section.

After selecting the pump and probe wavelengths, a sequential series of power sweeps is performed. First, an "Initialization Sweep" (Figs. 2(a), 2(d), 2(g), 2(j)), uses the HP configuration on an as-grown region to identify an "Initialization Setpoint" (P_I) for inducing crystallization with a characteristic rise in reflectance and clear plateau in the trend suggesting saturation of the crystalline phase. Next, an "Amorphization Sweep" (Figs. 2(b), 2(e), 2(h), 2(k)) is performed using the LP configuration on a region initialized with P_I to determine the "Amorphous Setpoint" (P_A) with a characteristic weak response at lower power densities followed by a gradual decrease in reflectance indicating reduced crystallinity consistent with the amorphous state. Here, the setpoint must be carefully chosen to avoid failure, which can be quantitatively noted by deviations in the slope of the crystalline to amorphous OTT diagram. A "Crystallization Sweep" (Figs. 2(c), 2(f), 2(i), 2(l)) is conducted using the HP configuration on a region previously initialized and amorphized with P_I and P_A. This determines the "Dynamic setpoint" (P_D), corresponding to a minimal increase in crystallinity from the amorphous state, and "Binary setpoint" (P_B), representing full crystallization. These setpoints are indicated by the dashed vertical lines highlighting abrupt changes in the slope, representing the onset of crystallization and maximum crystallinity.

The OTT diagrams also reveal unique tradeoffs resulting from differences in substrate and PCC material. We observe that samples with SOI substrates have lower power setpoints than those on silicon, along with steeper transitions when transitioning between crystalline and amorphous phases. This behavior was expected due to the buried oxide layer in the SOI substrate reducing the thermal diffusivity compared to bulk silicon, allowing for more heat to be absorbed by the PCC rather than being dissipated into the substrate. We also observe that Sb_2Te_3 required more power for phase transitions than $Ge_2Sb_2Te_5$ regardless of substrate and exhibited a smaller decrease in power requirements when switching to an SOI substrate from bulk silicon. We believe this could be partly attributed to differences in the PCC layer thickness, where the Sb_2Te_3 layers are 5 nm thick as opposed to the $Ge_2Sb_2Te_5$ layers being 35 nm thick; this results in a relatively reduced optical cross section in the Sb_2Te_3, hindering absorption. Our experimental observations agree with trends predicted by simulation (Table 1) and represent the first reported measurement of phase transition diagrams on Sb_2Te_3.

Optical Materials EXPRESS

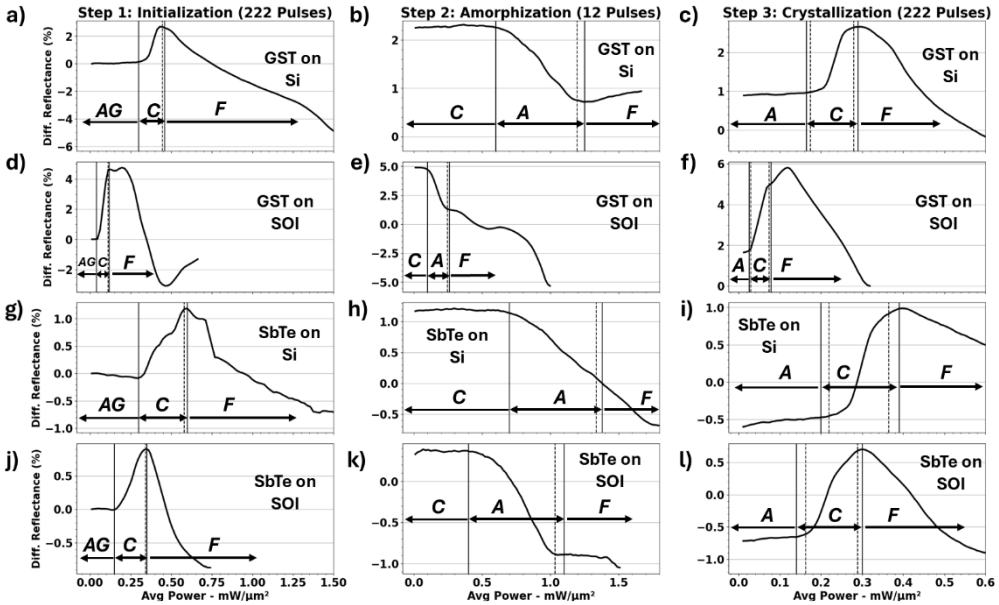

Fig. 2. Optothermal Transition Diagrams for $Ge_2Sb_2Te_5$ on Si (a-c), $Ge_2Sb_2Te_5$ on SOI(d-f), Sb_2Te_3 on Si(g-i), and Sb_2Te_3 on SOI(j-l). "AG", "A", "C", and "F" are phase diagram domains corresponding to "As Grown", "Amorphous", "Crystalline", and "Failure" states. Vertical Dashed lines indicate P_I, P_A, P_D, and P_B. Differential Reflectance (arbitrary units) is plotted against average power density of the near-infrared pump source.

3.1. Results: PCC programming and cycling

Using the power setpoints (P_I, P_A, and P_B) obtained from the OTT diagrams, we demonstrated optothermal cycling dynamics on both $Ge_2Sb_2Te_5$ and Sb_2Te_3. Each sample was initialized, then cycled using repeated exposures to HP and LP conditions at setpoints, with probe images captured after each exposure. The experimental procedure for cycling is illustrated in Fig. S10, where N_A and N_C denote the number of amorphous and crystalline exposures, respectively. Figure 3 reveals results of the optothermal cycling experiments, showing differential reflectance for the amorphous (blue) and crystalline (red) states. Optical contrasts shown in Fig. 3 are within the correct order of magnitude predicted by analytical reflection modeling shown in Fig. S8. All samples show an initialization region in the OTT diagrams which exhibit a downward drift in differential reflectance for both states at low cycle numbers, followed by a flattening of the trend representing stabilization at higher cycle numbers.

Among the four samples, $Ge_2Sb_2Te_5$ on SOI exhibited the lowest power requirements, while Sb_2Te_3 on SOI initialized with the least number of cycles, showing minimal signal loss while maintaining strong optical contrast. Sb_2Te_3 on silicon did not fully initialize until after 40 cycles, whereas $Ge_2Sb_2Te_5$ on silicon continued to drift through 100 cycles without clear stabilization. Both SOI-based samples showed reduced reflectance jitter compared with their silicon counterparts while preserving state contrast. Even after initialization, all samples exhibited a gradual drift toward lower reflectance and slight reflectance jitter under continued cycling. These results suggest that while some samples may not have reached their full initialization limit, the boundary between initialization and degradation, and the role of substrate and oxide cladding in determining it, remains an open question. Our data shows that PCCs on silicon substrates require more cycles to reach initialization when compared to PCCs on SOI substrates.

Optical Materials EXPRESS

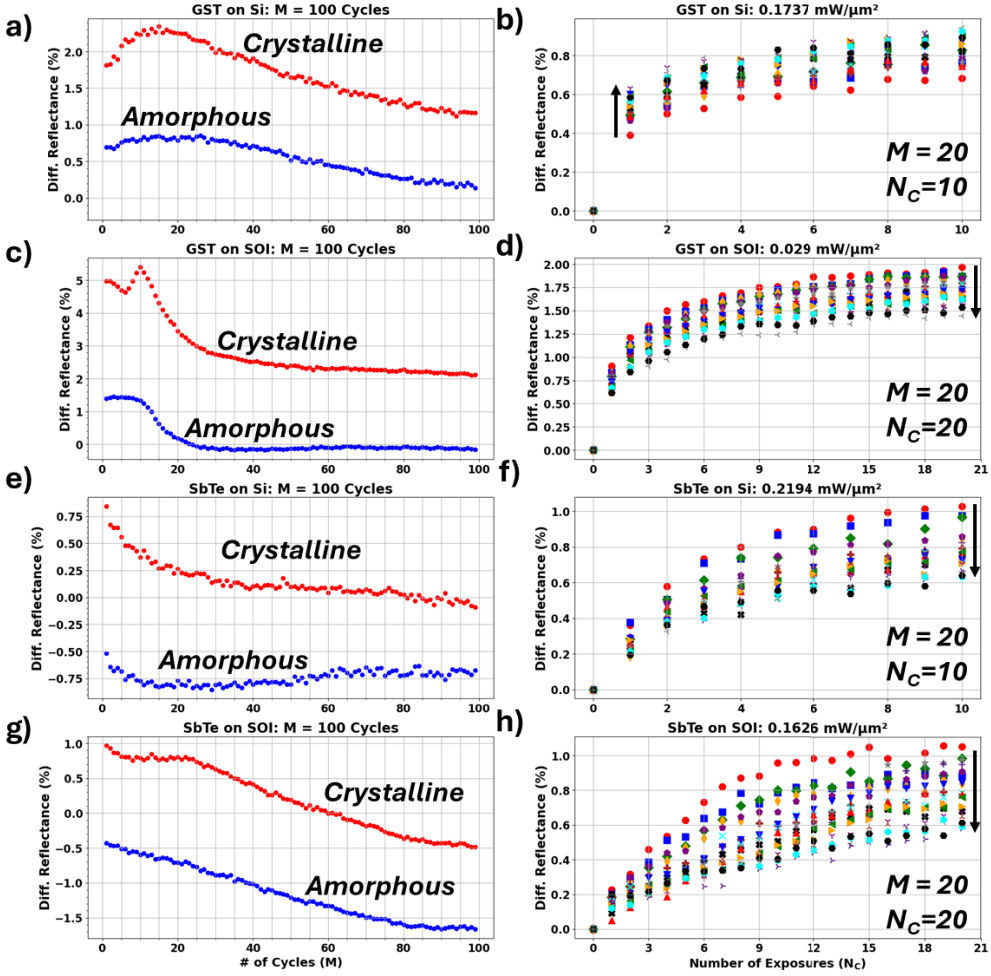

Fig. 3. Optothermal cycling (See Visualization 1) demonstrated on: **a)** 35 nm $Ge_2Sb_2Te_5$ on silicon substrate, **c)** 35 nm $Ge_2Sb_2Te_5$ on Silicon-on-Insulator substrate, **e)** 5 nm Sb_2Te_3 on silicon substrate, and **g)** 5 nm Sb_2Te_3 on Silicon-on-Insulator substrate. Reproducible Quasi-Analog states as a function of exposures of **b)** 35 nm $Ge_2Sb_2Te_5$ on Silicon at $P_D = 0.174\,mW/\mu m^2$, **d)** 35 nm $Ge_2Sb_2Te_5$ on Silicon-on-Insulator at $P_D = 0.029\,mW/\mu m^2$ **, f)** 5 nm Sb_2Te_3 on Silicon at $P_D = 0.219\,mW/\mu m^2$, and **h)** 5 nm Sb_2Te_3 on Silicon at $P_D = 0.163\,mW/\mu m^2$. Black arrows indicate the progression of cycles (Cycle 1-N_C).

Collectively, our observations indicate that substrate choice strongly influences phase transition dynamics.

We next examined how variations in the number of crystalline exposures (N_C) and incident power influence partial amorphous-to-crystalline transitions. To assess the effect of increasing N_C, we conducted cycling experiments as illustrated in Fig. S10, with $N_C >> 1$. For these results, we normalize differential reflectance to an amorphous baseline as opposed to the as-grown baseline used to normalize the OTT diagrams. Figures 3(b), 3(d), 3(f), and 3 h show differential reflectance of semi-crystalline states after repeated exposures at the dynamic crystalline setpoint. Our results reveal a logarithmic increase in differential reflectance with increasing number of exposures at the same power density without inducing failure. The optical contrast after many exposures exhibits a lower differential reflectance when compared to results obtained using the

Optical Materials EXPRESS

binary setpoint, indicating that repeated exposure alone cannot achieve full crystallization. We are the first to report cycling and the programming of analog states using Antimony Telluride (Sb_2Te_3). Next, we performed the same experiment while progressively increasing the incident average power on the $Ge_2Sb_2Te_5$ on SOI sample. Figure S10 illustrates this process with $N_A = 1$, $N_C = 20$, and $M = 16$, where average power ranged from 12.3 to 95.7 $\mu W/\mu m^2$, incrementing by 5.56 $\mu W/\mu m^2$ per cycle. The OTT diagrams shown in Fig. S11 reveal a linear rise in differential reflectance with increasing power, with failure occurring shortly after exceeding the binary crystallization setpoint (P_B).

Overall, results show that higher power density is required to access the full dynamic range of the amorphous to crystalline transition. Additionally, the number of accessible intermediate states decreased with increasing power, indicating that distinct combinations of average power (between P_D and P_B) and number of exposures must be used to maximize the number of achievable intermediate states. These programmable intermediate states highlight the potential for multi-level phase-change memory in integrated photonic systems.

4. Discussion: failure mechanisms

While our OTT diagrams enable selection of phase switching setpoints, it is difficult to discern between phase transitions and material failure solely through data obtained through reflectance imaging, with different failure mechanisms appearing as deviations in the slope of the OTT diagram (Fig. 4(a)). To address this, we qualitatively examine reflectance images near inflection points of our OTT diagrams to ensure that the selected power setpoints are not influenced by material failure.

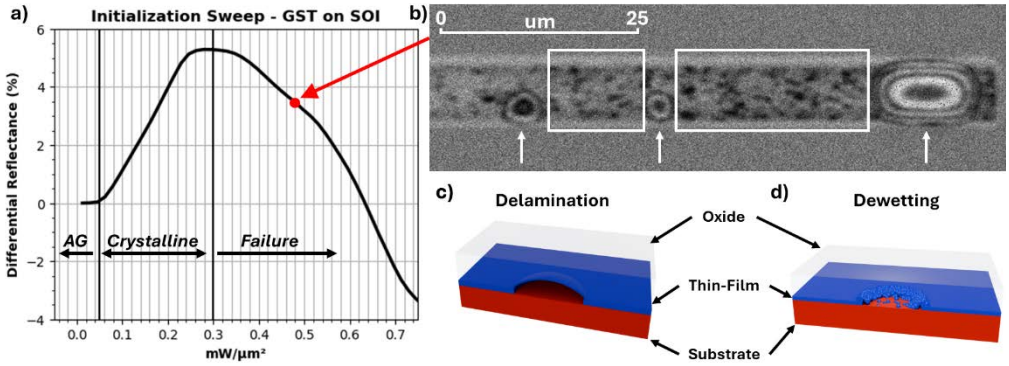

Fig. 4. **a)** Initialization Sweep on $Ge_2Sb_2Te_5$ on Silicon-on-Insulator Substrate that resulted in failure **b)** 480 nm Reflectance imaging of Dewetting (Boxed) and Delamination (Arrows) at point of failure (See Visualization 2 and Visualization 3) **c)** Cross-sectional Illustrations of Delamination and **d)** Dewetting

Ablation refers to the mechanism where the deposited thin film undergoes a solid to gas transition under very large optical power exposure causing the dielectric breakdown and vaporization from the substrate. The first way to mitigate this issue is to limit the maximum power exposure of the sample, however this is challenging because ablation can occur near the power density required to induce phase transition [33,46,47]. This is addressed by integrating an oxide cladding layer to all our material stacks, helping to prevent vaporization of the thin film when optically inducing phase change; this is common practice when creating PCC thin film stacks [48–52]. The scanning pattern of the beam can also greatly influence failure dynamics on the PCC thin film. For example, unidirectional rastering, where the beam scans across every line in the pixel grid in the same direction (i.e. left to right), introduces a non-uniform temperature gradient across

Optical Materials EXPRESS

the pixel grid, leading to significant mass flow lateral to the scanning direction of the beam, as observed in Visualization 4. This is addressed by introducing a Bi-Directional or "Serpentine" rastering pattern to reduce spatial temperature gradients, favoring a more uniform temperature across the scan area and discouraging failure mechanism effects.

Delamination refers to the changes in the adhesion across the thin film stack, resulting in poor thermal conduction and eventual loss in cyclability [52–55]. We believe this is driven by the build-up of stress in the thin film from non-uniform thermal expansion [53–56]. This failure mechanism, visualized in Fig. 4(b), with arrows pointing to delamination centers, appears as a fringe pattern due to optical thin film interference from a "bubble" that is formed in the thin film stack. This failure mechanism was not observed during cycling, when optimal transition parameters were used; and was most commonly observed when a sample was exposed to excessively high average power which creates larger temperature gradients.

Dewetting is observed when stress in the thin film causes the formation of "particles" and "voids" rather than maintaining a continuous layer on the substrate, severely impacting thin film uniformity which eventually degrades device performance [52,57]. This failure mechanism is visualized in Fig. 4(b), with boxes enclosing void sites, appearing as pinholes with dark spots with very little reflectance. We observe that dewetting typically does not occur from a single exposure, but rather over many exposures, with dewetting slowly appearing and increasing with the number of exposures over many cycles.

4.1. Discussion: multiphoton microscopy

The nonlinear optical response of PCCs provides insight into the relationship between their crystalline lattice structure, disorder, and symmetry as these materials transition between amorphous and crystalline states. Here, we employ Two-Photon Excitation Fluorescence (TPEF) and Second-Harmonic Generation (SHG) probes, which both require two photon absorption to produce emission. This absorption is enabled by the highly ordered lattice structure of the crystalline state, with non-linear emission from either probe suggesting crystallinity of our PCC. The nature of this emission (TPEF or SHG dominant) allows you to discern between dynamic transitions within the crystalline phase, as these processes rely on different energy pathways for emission. Variations in these probes imply a structural change in the PCC thin film.

Second-Harmonic Generation (Fig. 5(a)) is governed by inversion symmetry of the PCCs crystalline lattice, resulting in a narrow band emission at exactly one-half of the probe wavelength [58]. The effective medium of amorphous PCCs is centrosymmetric, whereas highly ordered crystalline PCCs introduce long-range order and breaks inversion symmetry, enabling stronger SHG emission [59–62]. Alternatively, Two-Photon Florescence Excitation (Fig. 5(b)) is particularly sensitive to defects in the crystalline structure, resulting in a broad band emission at a lower wavelength than the probe wavelength [58]. Lattice defects can increase the density of virtual states, facilitating broadband radiative recombination (see Fig. 5(b), Step 2), enabling stronger TPEF emission [3,58,63–74]. The formation of a highly ordered lattice, with a reduced number of defects, reduces the density of virtual states [75] resulting in a decrease in TPEF emission and an increase in SHG emission.

Figures 5(c) and 5(d) show reflectance and TPEF images of patterned $Ge_2Sb_2Te_5$. Here, we see that our multiphoton images are less sensitive to artifacts created by failure mechanisms and extrinsic materials parameters; they are seen in the reflectance image (Fig. 5(c)) but not in the TPEF image (Fig. 5(d)), demonstrating the reduction of thin film interference effects on probe data. This technique allows us to qualitatively differentiate between phase transitions and material failure. This technique also allows us to utilize our pump source for optical probing, combining a two-step pump-probe process into a single step. Because the probe emission occurs relatively far from the pump source, risk of optical crosstalk is minimal. This technique offers

Optical Materials EXPRESS

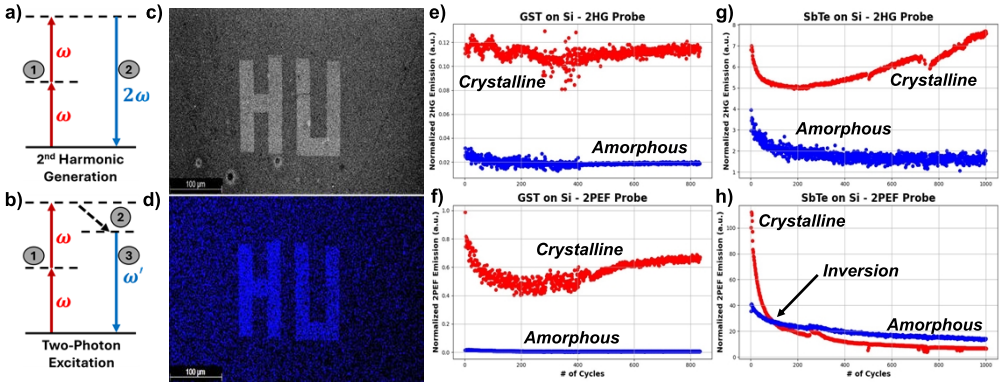

Fig. 5. **a)** SHG Energy Level Diagram. Two photons simultaneously interact with the PCC thin film in a virtual state (step 1) and are reemitted as a single photon at half the incident wavelength (Step 2). **b)** TPEF Energy Level Diagram. Two photons are simultaneously absorbed, promoting an electron to excited state S_2 (Step 1). The electron relaxes to state S_2 (Step 2). Lastly, the electron decays through photoluminescence (solid line), returning to the ground state S_0 (Step 3). **c)** Reflectance Image and **d)** TPEF Image of a crystalline 'HU' patterned into 35 nm $Ge_2Sb_2Te_5$ on Silicon. Cycling of $Ge_2Sb_2Te_5$ on Silicon using **e)** 2nd Harmonic Generation (SHG) and **f)** Two-Photon Excitation Florescence (TPEF) probes. Both probes were excited at 800 nm with photodetectors fixed to 398-403 nm and 575-605 nm respectively. Cycling of Sb_2Te_3 on Silicon using **g)** SHG and **h)** TPEF probes. Both probes were excited at 920 nm with photodetectors fixed to 456-464 nm and 610-710 nm respectively.

considerable experiment speedup (~2.28x improvement in cycling acquisition time) and reduced setup complexity, only requiring a single pulsed laser source.

Figures 5(e)-(h) show optical cycling results using this single step pump-probe technique. The HP configuration delivers far more pulses per pixel and thus higher intensity dose than the LP configuration. Because the non-linear responses scale with the square of intensity and dwell time rather than total power, the HP configuration produces much larger non-linear signals than the LP configuration [51]. Using this technique in conjunction with proper normalization for differing spatial light modulation configurations, we were able to obtain M = 830 Cycles on $Ge_2Sb_2Te_5$ on Silicon and M = 1000 cycles on Sb_2Te_3 on Silicon with clear and consistent optical contrast between phases shown in both the TPEF and SHG signals. Trends in the $Ge_2Sb_2Te_5$ data show initialization drift and jitter similar to that seen in reflectance cycling demonstrations, however, the sample appears to settle into consistent states at M < 400 Cycles. This implies that proper sample initialization may take hundreds of cycles, highlighting the utility of this single step technique. We observe minimal change in the non-linear response of the crystalline phase, implying consistent lattice structure of the crystalline phase when cycling.

For Sb_2Te_3 (Fig. 5(h)), an inversion in state contrast is observed at ~100 cycles. The observed decrease in crystalline state TPEF emission, and increase in SHG emission, may arise from a dramatic restructuring of the crystalline phase during initialization of the thin film, with the crystalline phase transitioning from a defect dominated structure to a more highly ordered crystalline structure. As the material initializes, the formation of a more highly ordered lattice in the crystalline phase reduces the density of virtual states, suppressing radiative relaxation, resulting in a decrease in TPEF emission and increase in SHG emission. Our non-linear probes for Sb_2Te_3 (Figs. 5(g) and 5(h)) reveal inverse trends in the crystalline state, one decreasing and the other increasing, while the reflectance probe (Fig. 3(e)) shows consistent crystalline phase contrast with the amorphous state, emphasizing the utility of non-linear optical probes

Optical Materials EXPRESS

when characterizing phases of PCC thin films. For all samples, we observe consistent minimal non-linear responses in the amorphous phase. We are the first to demonstrate phase diagrams of the non-linear response revealing dynamic PCC behavior in the crystalline phase.

5. Conclusion

We have demonstrated a fully optical, confocal microscopy–based platform for the intrinsic characterization and programmable control of phase-change chalcogenide thin films through spatial light modulation. By constructing Optothermal Transition (OTT) diagrams, we directly map phase boundaries, semi-crystalline regimes, and failure domains as a function of incident optical power, revealing clear substrate-dependent tradeoffs between silicon and silicon-on-insulator platforms. This approach enables reproducible identification of crystallization and amorphization setpoints, as well as stable access to intermediate optical states essential for multilevel photonic memory.

Beyond linear reflectance measurements, the incorporation of two-photon excitation fluorescence and second-harmonic generation microscopy provides a powerful nonlinear probe that distinguishes phase change from degradation and uncovers dynamic restructuring within the crystalline phase itself. These nonlinear signatures reveal behaviors that are not apparent through reflectance alone, including defect-mediated initialization dynamics and lattice ordering during extended cycling. Notably, this work presents the first experimental demonstration of OTT diagrams, reversible cycling, and analog state programming in Sb_2Te_3, an underexplored yet promising phase-change material for photonic applications.

Overall, this work establishes spatial light modulated confocal microscopy as a scalable and experimentally accessible tool for PCC characterization, optothermal programming, and materials discovery. The methodology is broadly applicable to a wide range of optical phase-change materials and thin-film stacks, offering a direct pathway toward the development of robust photonic memory, neuromorphic computing elements, and reconfigurable integrated photonic systems.

Funding. U.S. National Science Foundation (2329090); Research Foundation - Flanders (1S59025N).

Acknowledgements. We are grateful to Carlos A. Rios Ocampo and Chih-Yu Lee for their valuable feedback and ongoing support. We also thank Anastas Popratiloff and the members of the George Washington University Nanofabrication and Imaging Center (GWNIC) for providing access to laboratory facilities and technical assistance throughout this work. Additionally, we acknowledge use of the IBM HBCU Quantum Center funding support for this work.

Disclosures. The authors declare no conflicts of interest.

Data Availability. The data that support the plots within this paper and other findings of this study are available from the corresponding author upon reasonable request.

Supplemental document. See Supplement 1 for supporting content.

References

1. M. S. Nisar, X. Yang, L. Lu, *et al.*, "On-chip integrated photonic devices based on phase change materials," Photonics **8**(6), 205 (2021).
2. C. Ríos, M. Stegmaier, P. Hosseini, *et al.*, "Integrated all-photonic non-volatile multi-level memory," Nat. Photonics **9**(11), 725–732 (2015).
3. M. Wuttig and N. Yamada, "Phase-change materials for rewriteable data storage," Nat. Mater. **6**(11), 824–832 (2007).
4. J. Wen, J. Jiang, J. Ma, *et al.*, "The State-of-the-Art Phase-Change Integrated Photonic Devices With Electrically Driven Microheaters," IEEE Trans. Electron Devices **71**(2), 955–964 (2024).
5. R. E. Simpson, P. Fons, A. V. Kolobov, *et al.*, "Interfacial phase-change memory," Nat. Nanotechnol. **6**(8), 501–505 (2011).
6. I. Chakraborty, G. Saha, A. Sengupta, *et al.*, "Toward Fast Neural Computing using All-Photonic Phase Change Spiking Neurons," Sci. Rep. **8**(1), 12980 (2018).
7. S. Hu, C. Wang, S. Du, *et al.*, "Laser-induced reconfigurable wavefront control with a structured $Ge_2Sb_2Te_5$-based metasurface," Commun. Phys. **7**(1), 346 (2024).

Optical Materials EXPRESS

8. Q. Meng, X. Chen, W. Xu, *et al.*, "High Q Resonant Sb_2S_3-Lithium Niobate Metasurface for Active Nanophotonics," Nanomaterials **11**(9), 2373 (2021).
9. M. Delaney, I. Zeimpekis, H. Du, *et al.*, "Nonvolatile programmable silicon photonics using an ultralow-loss Sb_2 Se_3 phase change material," Sci. Adv. **7**(25), eabg3500 (2021).
10. M. Rudé, J. Pello, R. E. Simpson, *et al.*, "Optical switching at 1.55 μ m in silicon racetrack resonators using phase change materials," Appl. Phys. Lett. **103**(14), 141119 (2013).
11. J. Li, Y. Yun, K. Xu, *et al.*, "Performance Limits of Phase Change Integrated Photonics," IEEE J. Select. Topics Quantum Electron. **30**(4), 1–9 (2024).
12. C. Wu, Z. Jiao, H. Deng, *et al.*, "Reconfigurable inverse-designed phase-change photonics," APL Photonics **10**(1), 016113 (2025).
13. N. Q. Adanan, S. Wredh, M. A. Rahman, *et al.*, "Continuously tunable optical states of highly textured Sb_2Te_3," Opt. Mater. Express **15**(9), 2289 (2025).
14. S. Li, H. Huang, W. Zhu, *et al.*, "Femtosecond laser-induced crystallization of amorphous Sb_2Te_3 film and coherent phonon spectroscopy characterization and optical injection of electron spins," J. Appl. Phys. **110**(5), 053523 (2011).
15. G. A. Sevison, J. A. Burrow, H. Guo, *et al.*, "Wavelength and power dependence on multilevel behavior of phase change materials," AIP Adv. **11**(8), 085327 (2021).
16. X. Wang, H. Qi, X. Hu, *et al.*, "Advances in Photonic Devices Based on Optical Phase-Change Materials," Molecules **26**(9), 2813 (2021).
17. Y. Gutiérrez, S. Espinoza, M. Zahradník, *et al.*, "Characterizing optical phase-change materials with spectroscopic ellipsometry and polarimetry," Thin Solid Films **763**, 139580 (2022).
18. M. Hase, P. Fons, K. Mitrofanov, *et al.*, "Femtosecond structural transformation of phase-change materials far from equilibrium monitored by coherent phonons," Nat. Commun. **6**(1), 8367 (2015).
19. J. A. Burrow, R. G. Lawandi, A. Sarangan, *et al.*, "Electrically addressable tungsten doped phase change device in a through pixel configuration," Opt. Mater. Express **13**(4), 1131 (2023).
20. S. Guerin, B. Hayden, D. W. Hewak, *et al.*, "Synthesis and Screening of Phase Change Chalcogenide Thin Film Materials for Data Storage," ACS Comb. Sci. **19**(7), 478–491 (2017).
21. K. Bai, T. L. Tan, P. S. Branicio, *et al.*, "Time-temperature-transformation and continuous-heating-transformation diagrams of $GeSb_2Te_4$ from nanosecond-long ab initio molecular dynamics simulations," Acta Mater. **121**, 257–265 (2016).
22. N. Amini, J. Pries, Y. Cheng, *et al.*, "Thermodynamics and kinetics of glassy and liquid phase-change materials," Mater. Sci. Semicond. Process. **135**, 106094 (2021).
23. H.-D. Dong, M.-X. Chen, P. Zhang, *et al.*, "Ultrafast isothermal measurement of time-temperature-transition curve for critical nucleation in amorphous matrix," TIMS **3**(4), 100163 (2025).
24. S. A. Vitale, P. Miller, P. Robinson, *et al.*, "Phase Transformation and Switching Behavior of Magnetron Plasma Sputtered $Ge_2Sb_2Se_4Te$," Adv. Photonics Res. **3**(10), 2200202 (2022).
25. M. S. Alam, R. Laing, Z. Bolatbek, *et al.*, "Fast Cycling Speed with Multimillion Cycling Endurance of Ultra-Low Loss Phase Change Material (Sb_2 Se_3) by Engineered Laser Pulse Irradiation," Adv. Funct. Materials **34**(14), 2310306 (2024).
26. C. Laprais, C. Zrounba, J. Bouvier, *et al.*, "Reversible Single-Pulse Laser-Induced Phase Change of Sb_2 S_3 Thin Films: Multi-Physics Modeling and Experimental Demonstrations," Adv. Opt. Mater. **12**(28), 2401214 (2024).
27. K. Zhao, W. Han, Z. Han, *et al.*, "Ultrafast laser-induced integrated property–structure modulation of Ge_2 Sb_2 Te_5 for multifunction and multilevel rewritable optical recording," Nanophotonics **11**(13), 3101–3113 (2022).
28. J. Zheng, A. Khanolkar, P. Xu, *et al.*, "GST-on-silicon hybrid nanophotonic integrated circuits: a non-volatile quasi-continuously reprogrammable platform," Opt. Mater. Express **8**(6), 1551 (2018).
29. V. Weidenhof, I. Friedrich, S. Ziegler, *et al.*, "Laser induced crystallization of amorphous Ge_2 Sb_2 Te_5 films," J. Appl. Phys. **89**(6), 3168–3176 (2001).
30. S. M. Wiggins, J. Solis, and C. N. Afonso, "Influence of pulse duration on the amorphization of GeSb thin films under ultrashort laser pulses," Appl. Phys. Lett. **84**(22), 4445–4447 (2004).
31. J. Siegel, W. Gawelda, D. Puerto, *et al.*, "Amorphization dynamics of Ge_2 Sb_2 Te_5 films upon nano- and femtosecond laser pulse irradiation," J. Appl. Phys. **103**(2), 023516 (2008).
32. Z. Fang, R. Chen, J. E. Fröch, *et al.*, "Nonvolatile Phase-Only Transmissive Spatial Light Modulator with Electrical Addressability of Individual Pixels," ACS Nano **18**(17), 11245–11256 (2024).
33. S. Abdollahramezani, O. Hemmatyar, M. Taghinejad, *et al.*, "Electrically driven reprogrammable phase-change metasurface reaching 80% efficiency," Nat. Commun. **13**(1), 1696 (2022).
34. H. Zhang, L. Zhou, J. Xu, *et al.*, "Nonvolatile waveguide transmission tuning with electrically-driven ultra-small GST phase-change material," Sci. Bull. **64**(11), 782–789 (2019).
35. S. Ran, E. Petroni, L. Laurin, *et al.*, "Phase transitions and chemical segregation in Ge-rich GST based phase change memory cells," Sci. Rep. **15**(1), 11357 (2025).
36. A. Patil, Y. Le-Friec, P. Roussel, *et al.*, "Thermal characterization of Ge-rich GST thin films for phase change memories by Raman thermometry," J. Appl. Phys. **136**(17), 175102 (2024).
37. A. A. Burtsev, N. N. Eliseev, V. A. Mikhalevsky, *et al.*, "Physical properties' temperature dynamics of GeTe, Ge_2 Sb_2 Te_5 and Ge2Sb2Se4Te1 phase change materials," Mater. Sci. Semicond. Process. **150**, 106907 (2022).

Optical Materials EXPRESS

38. T. Kato and K. Tanaka, "Electronic Properties of Amorphous and Crystalline Ge_2 Sb_2 Te_5 Films," Jpn. J. Appl. Phys. **44**(10R), 7340 (2005).
39. S. A. Kozyukhin, A. A. Sherchenkov, E. V. Gorshkova, *et al.*, "Structural transformations in thin Ge2Sb2Te5 films," Inorg. Mater. **45**(4), 361–365 (2009).
40. Q. Li, J. Wei, H. Sun, *et al.*, "Temperature dependent thermal conductivity and transition mechanism in amorphous and crystalline Sb2Te3 thin films," Sci. Rep. **7**(1), 13747 (2017).
41. L. F. Mashadieva, J. O. Kevser, I. I. Aliev, *et al.*, "Phase Equilibria in the Ag2Te-SnTe-Sb_2Te_3 System and Thermodynamic Properties of the $(2SnTe)_{1-x}$ $(AgSbTe_2)_x$ Solid Solution," J. Phase Equilib. Diffus. **38**(5), 603–614 (2017).
42. Y. R. Guo, F. Dong, C. Qiao, *et al.*, "Structural signature and transition dynamics of Sb_2 Te_3 melt upon fast cooling," Phys. Chem. Chem. Phys. **20**(17), 11768–11775 (2018).
43. S.-M. Huang, J.-L. Hung, M. Chou, *et al.*, "The Highly Uniform Photoresponsivity from Visible to Near IR Light in Sb_2Te_3 Flakes," Sensors **21**(4), 1535 (2021).
44. M. N. R. Ashfold, F. Claeyssens, G. M. Fuge, *et al.*, "Pulsed laser ablation and deposition of thin films," Chem. Soc. Rev. **33**(1), 23 (2004).
45. W. Zhou, Z. Zhang, Q. Zhang, *et al.*, "Transient Study of Femtosecond Laser–Induced Ge_2 Sb_2 Te_5 Phase Change Film Morphology," Micromachines **12**(6), 616 (2021).
46. Q. He, Z. Liu, Y. Lu, *et al.*, "Low-loss ultrafast and nonvolatile all-optical switch enabled by all-dielectric phase change materials," iScience **25**(6), 104375 (2022).
47. J. Liang, G. Chen, X. Niu, *et al.*, "Enhanced surface effects and optical property modulation of Ge_2 Sb_2Te_5 by pulsed laser irradiation," Opt. Mater. Express **13**(3), 566 (2023).
48. T. Y. Teo, N. Li, L. Y. M. Tobing, *et al.*, "Capping Layer Effects on Sb_2S_3 -Based Reconfigurable Photonic Devices," ACS Photonics **10**(9), 3203–3214 (2023).
49. C. Wu, H. Deng, Y.-S. Huang, *et al.*, "Freeform direct-write and rewritable photonic integrated circuits in phase-change thin films," Sci. Adv. **10**(1), eadk1361 (2024).
50. C. C. Popescu, K. Aryana, B. Mills, *et al.*, "Understanding and Circumventing Failure Mechanisms in Chalcogenide Optical Phase Change Material $Ge_2Sb_2Se_4Te$," Adv. Opt. Mater. **13**(8), 2402751 (2025).
51. X. Zhou, W. Dong, H. Zhang, *et al.*, "A zero density change phase change memory material: GeTe-O structural characteristics upon crystallisation," Sci. Rep. **5**(1), 11150 (2015).
52. S. Loubriat, D. Muyard, F. Fillot, *et al.*, "GeTe phase change material and Ti based electrode: Study of thermal stability and adhesion," Microelectron. Eng. **88**(5), 817–821 (2011).
53. G. S. Syed, M. L. Gallo, and A. Sebastian, "Phase-Change Memory for In-Memory Computing," Chem. Rev. **125**(11), 5163–5194 (2025).
54. Y. Won, J. Lee, M. Asheghi, *et al.*, "Phase and thickness dependent modulus of Ge_2 Sb_2Te_5 films down to 25 nm thickness," Appl. Phys. Lett. **100**(16), 161905 (2012).
55. X. Fang, M. A. Masud, G. Piazza, *et al.*, "Interface dewetting as a source of void formation and aggregation in phase change nanoscale actuators," Appl. Phys. Lett. **122**(5), 051602 (2023).
56. P. T. C. So, C. Y. Dong, B. R. Masters, *et al.*, "Two-photon excitation fluorescence microscopy," (n.d.).
57. M. Zhu, S. Abdollahramezani, C. Li, *et al.*, "Dynamically tunable second-harmonic generation using hybrid nanostructures incorporating phase-change chalcogenides," Nanophotonics **11**(11), 2727–2735 (2022).
58. T. Liu, X. Fang, and S. Xiao, "Tuning nonlinear second-harmonic generation in AlGaAs nanoantennas via chalcogenide phase change material," Phys. Rev. B **104**(19), 195428 (2021).
59. B. Burganov, V. Ovuka, M. Savoini, *et al.*, "Ultrafast modulation of covalency in GeTe driven by a ferroelectric soft mode," (n.d.).
60. P. Nukala, M. Ren, R. Agarwal, *et al.*, "Inverting polar domains via electrical pulsing in metallic germanium telluride," Nat. Commun. **8**(1), 15033 (2017).
61. H. Ranawat, S. Pal, and N. Mazumder, "Recent trends in two-photon auto-fluorescence lifetime imaging (2P-FLIM) and its biomedical applications," Biomed. Eng. Lett. **9**(3), 293–310 (2019).
62. X. Zhu, H. Xu, Y. Liu, *et al.*, "Two-Photon Up-Conversion Photoluminescence Realized through Spatially Extended Gap States in Quasi-2D Perovskite Films," Adv. Mater. **31**(49), 1901240 (2019).
63. J. Kellner, G. Bihlmayer, M. Liebmann, *et al.*, "Mapping the band structure of GeSbTe phase change alloys around the Fermi level," Commun. Phys. **1**(1), 5 (2018).
64. S. Raoux, W. Wełnic, and D. Ielmini, "Phase Change Materials and Their Application to Nonvolatile Memories," Chem. Rev. **110**(1), 240–267 (2010).
65. S. Liu, J. Wei, and F. Gan, "Optical nonlinear absorption characteristics of crystalline Ge_2 Sb_2 Te_5 thin films," J. Appl. Phys. **110**(3), 033503 (2011).
66. J.-B. Dory, C. Castro-Chavarria, A. Verdy, *et al.*, "Ge–Sb–S–Se–Te amorphous chalcogenide thin films towards on-chip nonlinear photonic devices," Sci. Rep. **10**(1), 11894 (2020).
67. P. Pradhan, P. Khan, J. R. Aswin, *et al.*, "Quantification of nonlinear absorption in ternary As-Sb-Se chalcogenide glasses," J. Appl. Phys. **125**(1), 015105 (2019).
68. E. A. Romanova, Y. S. Kuzyutkina, A. I. Konyukhov, *et al.*, "Nonlinear optical response and heating of chalcogenide glasses upon irradiation by the ultrashort laser pulses," Opt. Eng. **53**(7), 071812 (2014).

Optical Materials EXPRESS

69. K. Zhang, J. Lin, and Y. Wang, "Phase-selective fluorescence of doped Ge_2 Sb_2 Te_5phase-change memory thin films," Chin. Opt. Lett. **13**(12), 121601 (2015).
70. T. Wei, J. Wei, K. Zhang, *et al.*, "Grayscale image recording on Ge_2 Sb_2 Te_5 thin films through laser-induced structural evolution," Sci. Rep. **7**(1), 42712 (2017).
71. J. Liu, S. Liu, and J. Wei, "Origin of the giant optical nonlinearity of Sb_2Te_3 phase change materials," Appl. Phys. Lett. **97**(26), 261903 (2010).
72. J. C. Martinez, L. Lu, J. Ning, *et al.*, "The Origin of Optical Contrast in Sb_2Te_3 Based Phase-Change Materials," Physica Status Solidi (b) **257**(1), 1900289 (2020).
73. J. Secor, M. A. Harris, L. Zhao, *et al.*, "Phonon renormalization and Raman spectral evolution through amorphous to crystalline transitions in Sb_2Te_3 thin films," Appl. Phys. Lett. **104**(22), 221908 (2014).
74. K. Aryana, H. J. Kim, R. Md, *et al.*, "Optical and thermal properties of Ge_2 Sb_2 Te_5, Sb_2 Se_3, and Sb_2 S_3 for reconfigurable photonic devices [Invited]," Opt. Mater. Express **13**(11), 3277 (2023).
75. M. Kuwahara, O. Suzuki, T. Yagi, *et al.*, "Complex Refractive Index, Specific Heat Capacity, and Thermal Conductivity for Crystalline Sb–Te Alloys and ZnS–SiO_2 with Various Compositions at High Temperatures," Jpn. J. Appl. Phys. **52**(12R), 128003 (2013).